CCFE
CULHAM CENTRE FOR FUSION ENERGY

UK Atomic Energy Authority

UKAEA-CCFE-PR(19)33

R. B. Morales, S. Heuraux, R. Sabot, S. Hacquin

The reconstruction of hollow areas in the density profile from frequency swept reflectometry

The reconstruction of hollow areas in the density profile from frequency swept reflectometry

R. B. Morales, S. Heuraux, R. Sabot, S. Hacquin

This is a preprint of a paper submitted for publication in
Plasma Physics and Controlled Fusion

The reconstruction of hollow areas in the density profile from frequency swept reflectometry

R. B. Morales

E-mail: rennanmorales@gmail.com
United Kingdom Atomic Energy Authority, Culham Centre for Fusion Energy, Culham Science Centre, Abingdon, Oxon, OX14 3DB, UK
IJL, UMR 7198 CNRS, University of Lorraine, 54011 Nancy, France
Institute of Physics, University of Sao Paulo, Sao Paulo 05315-970, Brazil

S. Heuraux
IJL, UMR 7198 CNRS, University of Lorraine, Nancy 54011, France

R. Sabot
IRFM, CEA, Cadarache, Saint-Paul-lez-Durance, France

S. Hacquin
IRFM, CEA, Cadarache, Saint-Paul-lez-Durance, France
EUROfusion Programme Management Unit, Culham Science Centre, Culham OX14 3DB, United Kingdom

Abstract.
All density profile reconstruction techniques for both O-mode and X-mode are based on the assumption that the cut-off frequency profile is monotonic. However, there are many sources of perturbations to the plasma that generate hollow areas in the cut-off frequency profile, breaking the aforementioned assumption and causing a significant immediate reconstruction error that is not rapidly damped. Inside these hollow areas, the probing microwaves exhibit no specular reflections, so they are refereed to as blind areas. It is demonstrated that even though no reflections occur inside the blind areas, the higher probing frequencies that propagate through these areas carry information about them that can be used to estimate their size. The information used is the signature imprinted in the time-of-flight signal. In addition to the reconstruction algorithm not handling well non-monotonic profiles, the reconstruction algorithm is based on the WKB approximation of the reflectometer signal, which ignores all full-wave features that are present in experimental signals. The corresponding full-wave features are investigated here with the use of full-wave simulations in 1D, with a special attention paid to the perturbed frequency band. The simulated signals of excess time-of-flight, coming from sine shaped perturbations, are used to build a database of perturbation signatures on 5 dimensions of parameters. The database is then used in a synthetic example to invert the perturbation signature and determine its size. The same procedure is also demonstrated in experimental reflectometry data corresponding to a magnetic island during a Tore Supra discharge. The new adapted reconstruction scheme, when compared to the standard reconstruction, improved the description of the density profile inside the blind area and also over 10 cm after it. This technique is pioneer in describing blind areas. Further research will focus on refining its assumptions and broaden its applications.

1. Introduction

The FMCW (frequency-modulated continuous-wave) reflectometry diagnostic is a well established technique for density profile measurement with successful implementations on various medium and large size tokamaks, such as DIII-D [1], Tore Supra [2, 3], ASDEX Upgrade [4, 5] and JET [6]. Even though there has been significant improvements in the reflectometry hardware design [2, 7] and data extraction techniques [5, 8, 9] over the last two decades, the measured density profiles on fusion experiments still require improvements in the data analysis part in order improve the accuracy of the reconstructed profile. As an example, the LFS (Low Field Side) reflectometer being built for ITER has as its first operation priority to achieve a minimum radial accuracy of 5 mm [10]. Improving the accuracy on the reconstructed density profile also improves the accuracy of extracted parameters for physical studies such as MHD instabilities and turbulence. In addition, the high spatial and temporal resolution, combined with precise reconstruction techniques, makes reflectometry a promising diagnostic for real-time monitoring of the plasma in future reactors.

The data analysis for profile reflectometry can be divided into three topics: the initialization technique; the recursive profile reconstruction algorithm; and the description of blind areas.

On the initialization technique, in O-mode reflectometry, the edge plasma is not directly probed and an assumption is made for the edge density profile. On the other hand, in X-mode, the plasma is probed with a frequency below any cut-off frequency, and the probing frequency increases until the injected waves start to be reflected at a position with assumed $\omega_{prob} = \omega_{ce}(R)$, i.e. zero density. The position is estimated from the amplitude rise of the reflected signal. The initial investigation on the initialization technique is described in [11] based on 1D full-wave simulations and future research will tackle the turbulence and 3D geometrical effects using 3D full-wave simulations. The research in the initialization technique is paramount to improve the accuracy and stability of the reconstructed profiles. It is a complex topic that will be tackled in future dedicated papers.

The recursive profile reconstruction algorithm for O-mode is well-established and based on the Abel inversion [12, 13]. For X-mode, the density profile reconstruction algorithm published by Bottollier-Curtet [14] in 1987 has been the standard reconstruction algorithm ever since, with a later constant correction proposed in [15, 16], and a recent variable integration weight factor proposed in [17] demonstrated improved reconstruction stability and precision in the edge plasma, and allowed for faster profile reconstructions without loss of accuracy. For smooth monotonic profiles with low turbulence levels and accurate initialization, these techniques are very precise. The advantage of the X-mode technique is the ability to probe the plasma edge and regions with lower density gradients due to the increased gradient of the cut-off frequency.

Both O-mode and X-mode density profile reconstruction techniques rely on the assumption of a monotonic cut-off frequency profile. However, there are many sources of perturbations that generate hollow areas in the cut-off frequency profile, breaking the aforementioned assumption. Inside these hollow areas, the probing microwaves exhibit no specular reflections and thus they are refereed to as blind areas. Even though no reflections occur inside the blind areas, the higher probing frequencies that propagate through these areas carry information about them that can be used to estimate their size. The information used is the signature imprinted in the time-of-flight signal. The profile reconstruction techniques have never been adapted in these cases where the cut-off profile is non-monotonic. Many phenomena cause perturbations in the density profile that lead to blind areas in the cut-off frequency profile. The small scale turbulence fluctuations generate an overall change in the acquired phase signal and the inversion process of the fluctuation properties is investigated via a transfer function, as initially approached in [18] and more recent developments are found in [19]. For isolated perturbations, the signature in the reflectometer signal is related to the size of the perturbation. The spectrum of the phase signal can be used to describe the spatial structure of small scale fluctuations (in the order of the probing wavelength) [20]. In this situation, the probing electric field is still similar in magnitude compared to probing the unperturbed profile. On this paper, on the other hand, the focus is on bigger perturbations that introduce a valley in the density profile that is large enough such that the probing microwaves have no specular reflection inside the valley. These perturbations are out of the Born approximation validity and the probing electric field is no more similar in magnitude to the unperturbed

case. This situation can occur during massive gas and pellet injections [21], MHD activity [22] and in hollow profiles that emerge during the initiation of heating systems [23] or even due to relativistic effects [24].

Section 2 demonstrates the typical error induced by the blind area on the standard reconstruction algorithm. Then, section 3 shows a proof of concept in the WKB framework to demonstrate that it is possible to estimate the perturbation size. The additional impact due to the full-wave effects not being considered in the reconstruction algorithms is discussed in section 4 with the use of full-wave simulations in 1D. Next, section 5 describes the influences of the perturbation shape on the reflectometry time-of-flight signal. Sections 6 and 7 create and apply a reconstruction technique for the blind areas based on a database of perturbation signals on 5 dimensions of parameters.

2. Reconstruction error due to blind areas

If the reconstruction method does not incorporate identification and reconstruction tools for these blind regions, big discrepancies can appear in the reconstructed profile. An example is shown in figure 1 using a simulated phase under the WKB approximation as the input signal. For simplicity, only the right hand polarization of X-mode is shown, since the behavior is equivalent, it represents a case more complex than the O-mode and it collapses to the O-mode solution when the background magnetic field goes to zero. The magnetic field profile used is typical of Tore Supra with a low magnetic field strength of 2 T at the plasma center.

It is clear from figure 1 that the unmodified standard reconstruction algorithm is unable to reconstruct the density perturbation. Furthermore, if the oscillations are smoothed, the perturbation can be neglected entirely, or even worse, a shift can be introduced in the reconstructed profile after the perturbation if the time-of-flight jump is filtered out.

The density profile reconstruction algorithms developed in [15, 17] for X-mode reflectometry are based on linear integrations of the refractive index, except for [17] where the shape of the last integration step is optimized based on the local plasma parameters. Due to a sharp change of the refractive index near the cut-off position, the shape of the last integration step is the main factor that dictates the accuracy of the reconstructed profile. As explained in [17], the trapezoidal integration over all radial steps before the final radial step is always more accurate than the integration on the last step for smooth monotonic density profiles, unlike the profiles treated in this paper. Such disparity was initially predicted in [15]

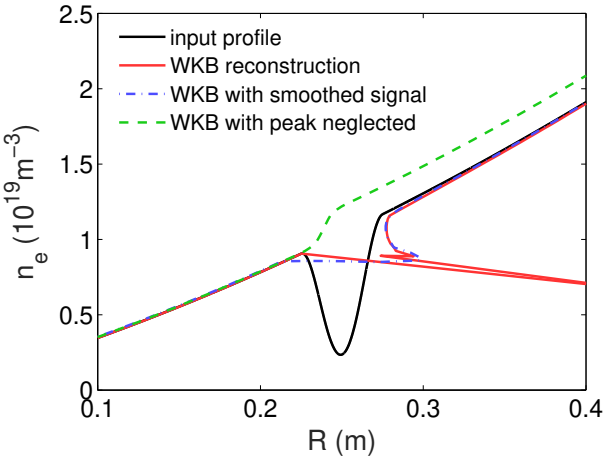

Figure 1. Synthetic example of input versus reconstructed density profiles with a blind area. The profile was reconstructed with the standard Bottollier-Curtet algorithm with a constant correction, as in [15–17], using three different treatments in the phase signal. The radial axis is defined from zero at the plasma edge and increasing towards the plasma center.

with the observation of refractive index profiles similar to those displayed in figure 2.

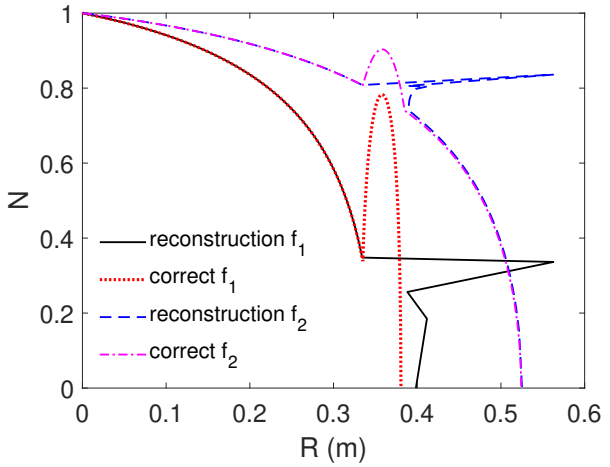

Figure 2. Calculated refractive index profiles (correct and reconstructed) for two different probing frequencies, f_1 and f_2, corresponding to two different cut-off positions, at 0.38 m and 0.52 m. The radial origin is at the plasma edge starting with zero density (hence $N(0) = 1$) and increasing towards the plasma center. A perturbation was introduced at the position of 0.36 m with a 5 cm width and a depth in the cut-off profile of 10 GHz. The conditions simulated correspond with typical Tore Supra parameters: plasma radius of 0,72 m and at the plasma core a magnetic field strength of 2.5 T and electronic density of 6×10^{19} m^{-3}.

The additional error on the reconstructed profile due to the error on the trapezoidal integration contributes for the large discrepancies on the recon-

structed density profiles observed in figure 1. As can be seen in figure 2, a probing frequency just above the blind area, f_1, undergo abrupt changes in the refractive index path, which leads to a poor discrete description of the correct refractive index along the perturbation during the reconstruction process. This discrepancy translates into a large error in the reflection position. As the probing frequency is increased, the perturbation on the refractive index path diminishes and the error caused in the reconstructed reflection position decreases, as can be observed for the probing frequency f_2.

Even though the probing microwaves are not reflected inside the blind region, there is information to be explored from the higher probing frequencies that propagate through the perturbation. The parameters necessary to describe a perturbation are: the perturbation width; the perturbation depth; and the perturbation shape. For simplicity, the first perturbations investigated have a well known shape and width and are inserted in a region with linear cut-off frequency profile, f_{cut}, which can be either f_{pe} when probing with O-mode or f_R if probing with the right-hand X-mode. In this way, the density profile can be reconstructed using an unperturbed signal, which experimentally could come from a previous sweep or an interpolation of the time-of-flight signal with the perturbation signature removed. Afterward, the perturbation signature is evaluated to determine its properties. To determine the perturbation depth, a signature in the time-of-flight signal is scaled to the perturbation depth (for an assumed width and shape).

As a proof of concept, this procedure is developed in the next section (section 3) for signals simulated using the WKB approximation. Afterward, the reflectometer signal is simulated with a 1D full-wave equation solver to take into account the full-wave effects, such as tunneling, wave-trapping, interference and scattering. Then, the influence of the perturbation shape on the perturbation signature is discussed, and lastly, the reconstruction techniques are discussed.

3. Blind area reconstruction proof of concept in WKB framework

In this section, a proof of concept is done using the simplest simulation of the measured phase signal, with the use of the WKB approximation. The right-hand X-mode case is considered for the computations and the result is compatible with the O-mode solution when the background magnetic field goes to zero. The WKB approximation that computes the wave's phase, ϕ, at each probing frequency, f_n, is presented in equation 1 [12]:

$$\phi\left(f_n\right) = \frac{2\pi f_n}{c}\int_{edge}^{R_n} N\left(f_n, f_{pe}(R), f_{ce}(R)\right) dR - \frac{\pi}{2}, \quad (1)$$

where c is the speed of light in vacuum, R_n is the reflection position for the probing frequency f_n and N is the refractive index given by equation 2:

$$N = \sqrt{1 - \frac{X(1-X)}{1-X-Y^2}}, \quad (2)$$

with

$$X = \frac{f_{pe}^2}{f_n^2}, \qquad Y = \frac{f_{ce}}{f_n}. \quad (3)$$

The WKB time-of-flight signal can be directly calculated taking the derivative of the phase signal with respect to the probing frequency.

The simplest solution to describe the blind area is to relate the jump amplitude in the time-of-flight signal when going through the valley, to the depth of the perturbation with an assumed shape and a fixed width. Figure 3 shows the time-flight signal computed under the WKB approximation for the input profile presented in figure 1.

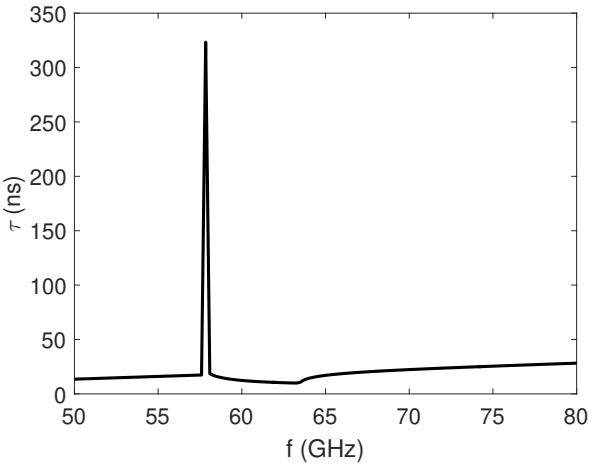

Figure 3. Time-of-flight during a right-hand X-mode sweep of the probing frequency, computed under the WKB approximation for the example conditions given in figure 1.

The height of the peak present in the time-of-flight signal can be directly related to the perturbation depth, as long as the perturbation width and shape are fixed and known. Figure 4 illustrates the relation obtained when inserting sine shaped perturbations with various depths and fixed width and radial position, on fixed profiles of f_{pe} and f_{ce}.

Using this relation, one can accurately reconstruct the perturbation that is inside of the boundary conditions assumed. After determining the unperturbed

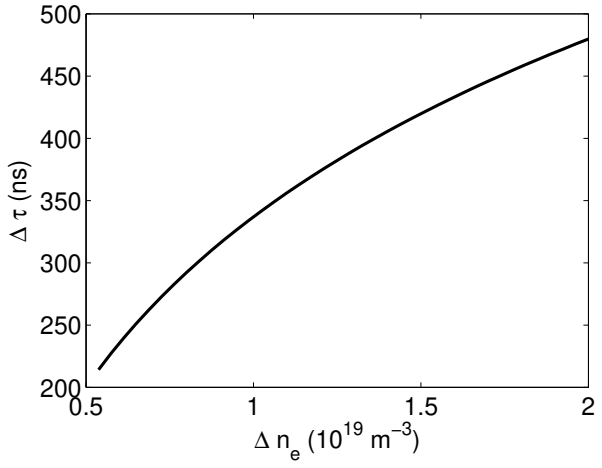

Figure 4. Relation of the time-of-flight jump to the depth of a sine shaped perturbation with a fixed width and radial position in the same conditions as introduced in figure 1.

profile from a previous frequency sweep or an interpolation of the time-of-flight skipping the perturbation, the perturbation is estimated with the relation in figure 4 and inserted back into the unperturbed profile. Initially skipping the perturbation's signature avoids the problem on the trapezoidal integration that is illustrated in figure 2.

Applying this procedure to the example case of figure 1 results in the reconstructed profile displayed in figure 5.

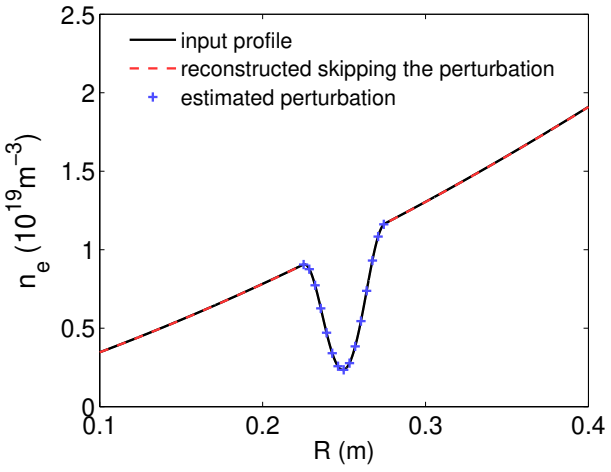

Figure 5. Input and reconstructed density profiles. The reconstructed profile is divided into a regular reconstruction skipping the perturbation, plus the estimated perturbation. The perturbation is estimated using the relation obtained for a sine shaped perturbation with a fixed width.

The procedure described above can successfully reconstruct the density profile of blind regions as long as the assumed boundary conditions are satisfied. However, the experimental signals are more complex than the signal computed under the WKB approximation. In the next sections, a full-wave 1D wave equation solver code is used to simulate the time-of-flight signals. Not only the WKB solution is out of its domain of validity in some parts, but in addition, time-dependent full-wave phenomena are present in the full-wave simulated signals. Therefore, these additional effects must be taken into account to build new relations like the one demonstrated in figure 4 to successfully reconstruct the profile of the blind areas with experimental signals. Moreover, these relations will vary with the perturbation parameters of shape and width, and the local profile parameters of ∇f_{cut} (the gradient of the cut-off profile) and f_{ce} in the X-mode case, thus, these dependencies are also taken into account.

4. Time dependent full-wave effects in the simulated signals

The profile reconstruction algorithms are based on the WKB approximation for the phase increment signal, therefore, it is essential to understand how the full-wave effects alter the WKB signal in order to avoid discrepancies in the reconstruction process. In addition, the full-wave effects can be used to extract additional characteristics of the shape of the blind area. Due to the complexity of this problem and the challenging task that it would be to extract these information from experimental signals, this approach is not tackled here and is left for further investigation as a refinement to the methods developed here. An initial introduction into considering some of these effects can be found in [25].

In order to investigate the full-wave effects from the blind regions covered here, the perturbations are introduced in a linear cut-off frequency profile (f_{cut}). Since the phase evolution depends not only on the density but also on the magnetic field for the X-mode, working in the f_{cut} framework allows to account for both the density and the magnetic field together. The O-mode solution is again included when the magnetic field goes to zero. Later on, the specific dependency on the f_{ce} profile is also taken into account when deducing the most general reconstruction technique. The dependency on f_{ce} becomes important when investigating perturbations near the plasma edge, where the density can be very low and f_{cut} approaches f_{ce}. Before then, the f_{ce} profile is fixed for all the following analyses of full-wave effects, focusing on perturbations in typical conditions of core plasma in Tore Supra. For such, the magnetic field strength is fixed at 3.2 T at the plasma

center and a standard tokamak 1/R radial dependency. The cut-off profile, f_{cut}, is assumed locally linear and the maximum density in the plasma center is $6 \times 10^{19} m^{-3}$. Consequently, the perturbations placed halfway between the plasma edge and the plasma center have density close to $3 \times 10^{19}\ m^{-3}$, magnetic field strength of 3 T, and are probed at around 105 GHz.

In this section, the perturbations are subtracted exclusively from the f_{cut} profile with a shape of one period of a sine squared function, and size in the scale much larger than the probing wavelength in vacuum. The sine squared shape was chosen for the studies of this section due to its characteristics of having null magnitude and derivative each half wavelength. This allows for smooth local implementation on top of the assumed profile. An example of such a perturbation is presented in figure 6, with 6.4 cm width and varying depth.

In order to account for the full-wave effects, the reflectometer signals are simulated with a 1D time-dependent full-wave code, based on a wave equation solver and a 4th order Runge-Kutta [26] approximation on the derivatives of fields and velocities [27]. The numerical reproduction of the reflectometer signal is a replica of the experimental set-up of a heterodyne IQ-detection scheme [7, 28] and the same data treatment with tomographic techniques [8, 9] for maximum compatibility. The instantaneous phase increment is directly extracted from the angle of the reflectometer simulated signal and the wave's amplitude from its modulus. In addition, the instantaneous time-of-flight signal is directly obtained by deriving the instantaneous phase with respect to the probing frequency. Apart from the instantaneous signals, a spectrogram can also be computed from the simulated signal to observe all its frequency components.

The simulated instantaneous time-of-flight signals corresponding to probing the profiles depicted in figure 6 can be found in figure 7. The chosen frequency sweeping rate was 20 GHz/μs, compatible to the system that was once installed in Tore Supra [29].

It can be seen in figure 7 how the height of the peak in time-of-flight is no longer a good scaling parameter to the perturbation depth, as done previously in section 3 when the phase is computed in the WKB framework. The reason is because of big fluctuations in the vicinity of the time-of-flight jump. Other features along the higher frequencies need to be explored in order to extract information from the perturbation size.

The procedure to reconstruct the blind area is tackled in section 6, because firstly, the full-wave effects are discussed in order to clarify all their features in the simulated signals. The full-wave effects discussed below are: interference, wave-trapping,

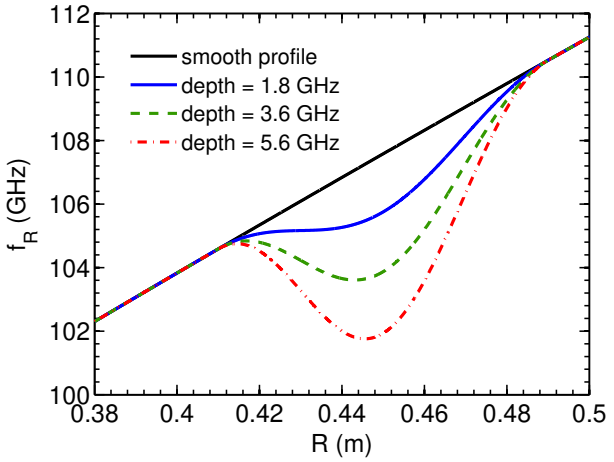

Figure 6. Linear f_{cut} profiles with sine square shaped valleys of different depths and a fixed width of 6.4 cm.

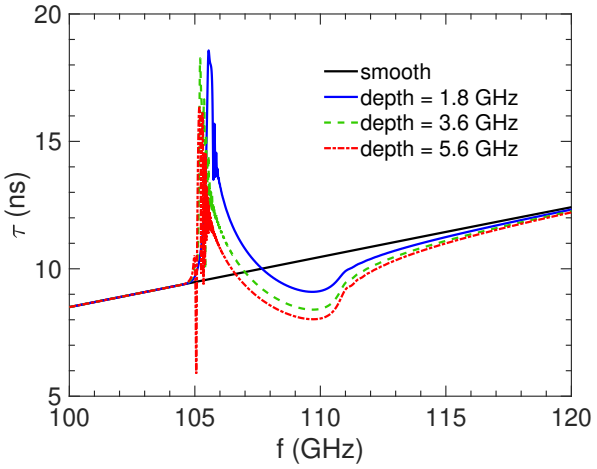

Figure 7. Instantaneous time-of-flight signals from probing the profiles introduced in figure 6 with a sweeping rate of 20 GHz/μs.

Bragg backscattering and tunneling. The impact of these effects are only briefly summarized here and a more detailed study of these effects can be found in [25], where the same simulation tools of this paper were used.

4.1. Interferences, wave trapping and resonances

The fluctuations around the time-of-flight jump are interferences due to the frequency mixing caused by the time-dependent effects around the perturbation. As the probing frequency is swept and arrives at the jump frequency, there will be a small band of frequencies that will partially tunnel into the valley. In the most complicated scenarios, the tunneling interfaces followed by the valley can act as a system of three

partially reflecting mirrors; two interfaces to entry and exit the tunneling barrier and another at the end of the valley. Between the three mirror system, specific frequencies can be trapped for a longer period and return mixed in the reflected signal. Frequency mixing also occurs when the plasma is probed just above the perturbation frequency. In this case, the probing wave propagates much slower through the perturbation because it is close to its cut-off frequency. Therefore, these slowly propagating frequencies arrive at the antenna after some slightly higher probing frequencies. All these effects contribute to the frequency mixing generating the interferences observed around the time-of-flight jump.

The interfaces between the tunneling boundaries and the valley can be interpreted as cavities that, in addition to the interferences mentioned above, can fulfill a resonance condition [30]. When this condition is satisfied, a positive or negative spike is seen in the time-of-flight signal at the resonant frequency. One example of a resonance can be observed in figure 7 for the signal corresponding to the perturbation depth of 5.6 GHz. The signal from a single perturbation can be observed on the spectrogram, as the example given in figure 8, for the smooth sine shaped perturbations with a 5 cm width and 5.6 GHz depth.

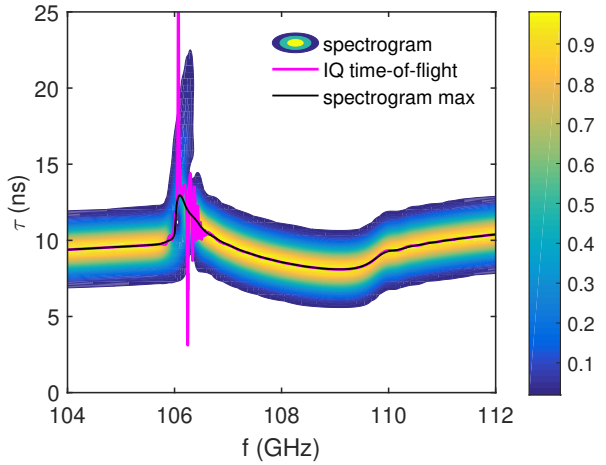

Figure 8. Spectrogram and instantaneous time-of-flight signals over a perturbation with sine square shape, 5 cm width and depth of 5.6 GHz.

The modulation and resonances are evident in these simulated signals (considering smooth sine shaped perturbations) but are very hard to identify and isolate in experimental data because of the innate noise level. Thus, the inversion technique is more robust if using a bigger bandwidth with the frequencies above the time-of-flight jump. In addition, the maximum of the spectrogram is the signal less sensitive to these modulations, compared to the instantaneous time-of-flight, as can be observed in figure 8. The interferences and resonances in the simulated signals affect the maximum of the spectrogram only over a bandwidth of 1 GHz on the probing frequency around the jump in time-of-flight.

The reflection coefficient of each interface in such three mirror system can be computed from the refractive index jump, according to [31]. Steep jumps in refractive index can also lead to strong Bragg backscattering for the probing frequencies above the perturbation. This effect is demonstrated analytically in [32]. In order to illustrate an academic example with strong wave trapping, resonance conditions and Bragg backscattering, a square perturbation with depth of 10 GHz is introduced in the f_{cut} profile. The corresponding signals are displayed in figure 9. The abrupt jump in f_{cut} enhances the reflections due to the abrupt refractive index jump and also because the squared edges have broad wavenumber spectra that end up fulfilling the Bragg condition for many probing frequencies.

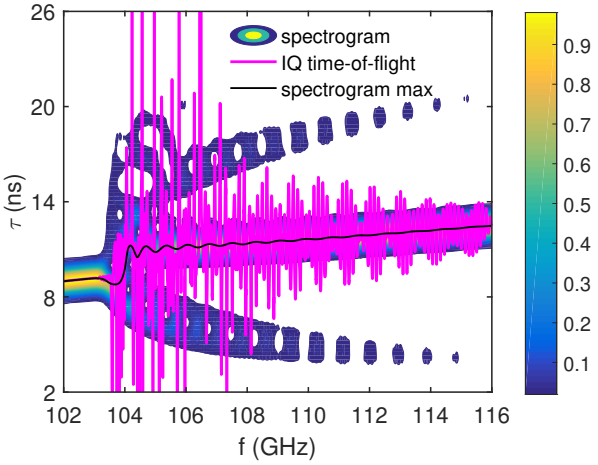

Figure 9. Spectrogram and instantaneous time-of-flight for the 10 GHz square valley in f_R.

The instantaneous time-of-flight signal in figure 9 shows many resonant frequencies and reflections. After the smoothed time-of-flight jump on the spectrogram, two additional oscillating branches arise. The upper branch belongs to waves that were trapped and arrive later in the reception antenna, and the lower branch belongs to reflections that occurred before the cut-off frequency, i.e. a Bragg backscattering component. The spectrogram maximum signal is still smooth and continuous but contain small fluctuations. In order to remove these additional contributions from the main reflection in the cut-off, one can use the tomography techniques to apply a narrow band filter that follows

the respective beat frequency evolution [8]. Although a square perturbation is not realistic, additional echoes are seen quite often experimentally and this analysis can be extended to these cases.

4.2. The amplitude signal and the tunneling effect

An additional information from the full-wave signal is the receiving wave amplitude extracted using the IQ detection method, as seen in figure 10 for the cases in figure 6.

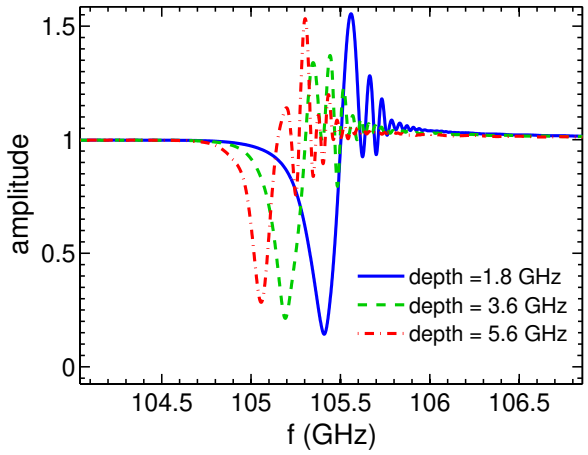

Figure 10. Amplitude from the simulated measurement when probing the profiles introduced in figure 6 with a sweeping rate of 20 GHz/μs.

The deep drop in the amplitude signals in figure 10 reveals the existence of a valley in f_{cut}, even in cases where no blind region is found. The amplitude drops are due to the electromagnetic flux conservation when probing a negative curvature that can lead or not to a blind area. Amplitude drops can also appear due to 3D geometrical effects, because unlike in 1D, the reflected waves in 3D not always fully return to the antenna. These effects are not seen here since the simulations performed are in 1D. Apart from the electromagnetic flux conservation and the geometrical effects, as the probing frequency approaches the jump over a blind region, the microwaves start to partially tunnel into the valley causing the received amplitude to decrease. The frequencies that partially tunneled into the perturbation eventually return to the antenna later on. This is why the amplitude drop is followed by an amplitude increase. When these delayed waves return to the antenna, they interfere with higher probing frequencies, which explains the fluctuations after the initial amplitude dip. The way these frequencies are mixed strongly depends on the quality factor of the cavities (inside the tunneling region and inside the valley) combined with the sweeping rate of the probing frequency. The quality factor dictates the interference amplitudes and the sweeping rate dictates the interference bandwidth. All the signals displayed in this paper have a fixed sweeping rate of 20 GHz/μs, which corresponds to the sweeping rate available in Tore Supra during the discharge studied in section 7. Faster sweeping rates extend the frequency band influenced by the full-wave effects, and if too high, an additional beat frequency is induced and the amplitude variations become more sensitive to the electromagnetic flux conservation due to the changes in the cut-off gradient.

The time at which the tunneled waves return is impossible to be accurately determined experimentally. The frequency at which the microwaves start tunneling, on the other hand, are related to the probing frequency and the tunneling barrier width. For the tunneled waves to be reflected back, they must have an evanescent path equal or longer than the width of the barrier to cross into the perturbation. The analytical expression for the fields of the evanescent wave is demonstrated in [31]. In practice, the tunneling band for the cases studied in this paper were verified for a varying perturbation width on a fixed perturbation amplitude of 15 GHz. The band of the amplitude drop until half of its original value was observed to be longer for the shortest perturbation width of 2 cm, being 1.25 GHz, and shorter for wider perturbations, like 0.6 GHz for the 6 cm width.

Apart from the interferences due to the wave-trapping in the cavities, additional reflections can emerge from Bragg backscattering when the spectrum of the inserted perturbation contains wave-numbers fulfilling the Bragg rule. In the end, the interferences can originate from one or many of these sources. The bandwidth at which these effects take place in the amplitude signals of figure 10 corresponds to the same bandwidth in their respective time-of-flight signals in figure 7. The amplitude of the incoming waves from the full-wave effects are normally small compared to the amplitude of the specular reflections from the cutoff positions. Therefore, as can be observed in figures 10 and 7, when the specular reflection dominates, even though some full-wave effects still exist, they have much lower amplitude and exert no influence in the time-of-flight signal. On the other hand, when the specular reflections are too weak or practically inexistent, the contribution from the full-wave effects dominate the time-of-flight signals.

Since the contribution from the full-wave effects were observed to be restricted to the bandwidth of the amplitude variations, the full-wave effects can be assumed limited to a bandwidth already observed for the tunneling effect. Furthermore, the interference contributions can be strongly suppressed

if the maximum of the spectrogram is taken as the time-of-flight signal instead of the instantaneous time-of-flight, as observed in figure 7. The tunneling effect contribution, on the other hand, is unavoidable in the spectrogram signal, but its presence is indicated by the dip in the amplitude signal.

To conclude on how the full-wave effects are tackled on the reconstruction process, figure 11 shows an example comparison between the time-of-flight extracted from the maximum of the spectrogram of the full-wave simulation versus the WKB simulated time-of-flight. This is a case where all full-wave effects are present within a bandwidth of 1 GHz around the time-of-flight jump. As long as a corresponding experimental signal is treated outside of this bandwidth, the experimental time-of-flight can be assumed well described by the WKB simulated signal. This conclusion is crucial for building a database of signals used to reconstruct the perturbations in section 6.

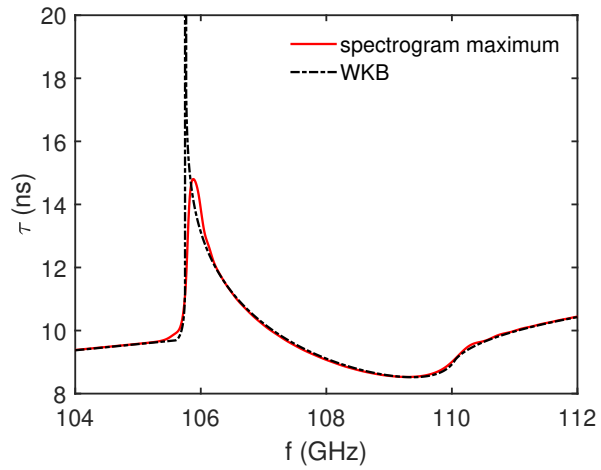

Figure 11. Comparison between a full-wave time-of-flight from the maximum of the spectrogram versus a WKB simulated time-of-flight over a perturbation with sine square shape, 5 cm width and depth of 5.6 GHz.

5. Influence of the perturbation shape on the time-of-flight signal

The observation of all full-wave effects demonstrate that there is much more information in the reflectometer signals than just the amplitude of the time-of-flight jump. Moreover, the time-of-flight signal is highly susceptible to interference fluctuations around the jump. Therefore, analyzing the higher frequency band becomes the most robust path. When exploring the time-of-flight signal in the higher probing frequencies, the signal is also dependent on the shape of the perturbation. This section summarizes the influence of the perturbation shape by investigating the impact on the time-of-flight signal by changing the perturbation skewness and kurtosis.

The skewness is an indication of the asymmetry of a distribution around its mean value. It is mathematically defined in [33]. To investigate the effect of the radial non-uniform contribution to the time-of-flight signal, the refractive index profile and the time-of-flight signal have been investigated in [25] for a probing frequency slightly higher than all cut-off frequencies in the blind area. The radially non-uniform refractive index distribution (same for the time-of-flight) inside the perturbation is caused by the radially non-uniform ratio of f_{pe} to f_{ce}, but it is only a higher order effect that can be neglected in the perturbation reconstruction techniques treated here.

The kurtosis of the perturbation is an indication if the perturbation is more concentrated in the center or in the extremities. A mathematical definition can be found in [34]. To investigate this effect, three perturbation shapes were investigated on a perturbation with a width of 12 cm. The shapes used were a sine function, a sine squared function, and a cubic sine function. For the sine function, the depth was set at 8 GHz but it increases for the other shapes in order to maintain a constant area on the f_{cut} profile, i.e. $\int_{width} f_{cut} dR = const.$ The resulting profiles can be observed in figure 12.

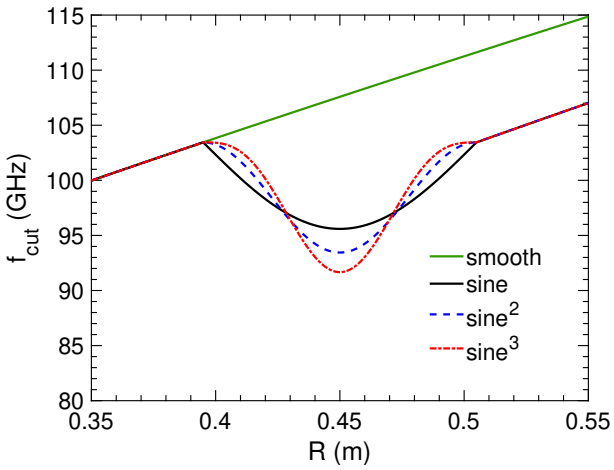

Figure 12. Perturbations with varying kurtosis over a linear f_{cut} profile.

In order to investigate the radial distribution of the time-of-flight contribution from the perturbation, figure 13 shows the time-of-flight differentiated radially for a single probing frequency corresponding to a cut-off just above the perturbation. This quantity was computed under the WKB approximation only for a qualitative observation, therefore all full-wave effects,

specially tunneling, are neglected. The total time-of-flight contribution for this single probing frequency after propagating through the blind area is given by the radial integral of the differential time-of-flight and is given in the legend of figure 13. The integral values show the observable differences in time-of-flight from the different perturbation shapes. These are qualitative observations because these differences are much higher at probing frequencies with cut-off close to the top of the perturbations and decrease when increasing the probing frequency. At these probing frequencies just above the perturbation the time-of-flight is strongly influenced by the full-wave effects discarded in these computations.

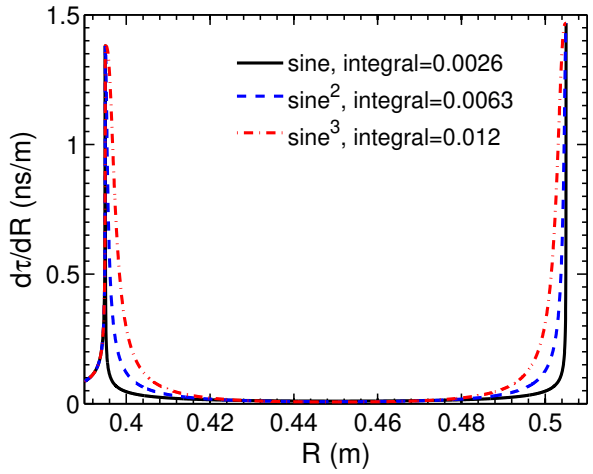

Figure 13. Differential time-of-flight per radius when probing with a frequency corresponding to a cut-off slightly above the perturbations of figure 12. The integral values in the legend is computed by integrating $d\tau$ over dR along the perturbation, thus it corresponds to time-of-flight contribution exclusively from the perturbation.

Figure 13 shows how the perturbations have a larger time-of-flight contribution from the regions with higher f_{cut}, i.e. in the borders of the perturbation, or equivalently, the more they are elongated if keeping a constant area. This happens because the probing waves propagate much slower when propagating with a probing frequency very close to the local cut-off frequency. The shapes selected for figure 13 are close to the expected real cases. The cubic sine shape have a very shallow borders and is only deep in the center. This would almost characterize it as a narrower valley. The sine shape on the other hand, is not so realistic because the edges are not smooth and have discontinuous derivatives. The data presented in figure 13 represent a single probing frequency slightly above the perturbation in order to emphasize the difference between the used shapes as should not be taken as the total difference between the entire signal coming from the perturbations. As mentioned before, the probing frequencies around the time-of-flight jump are neglected due to the tunneling and interference full-wave effects, and at the higher probing frequencies this effect is diminished.

In addition, as observed that the bottom of the perturbation have a much lower contribution to the additional time-of-flight, this effect raises another question. If the bottom of a valley perturbation has less impact on the time-of-flight, it means that the deeper the valley is, the less prominent becomes the signature of a given δf_{cut} at the bottom of the valley. This accuracy can be inferred by analyzing perturbations with different depth, and comparing the time-of-flight after the perturbation, with versus without an additional δf_{cut} of constant area in f_R. The perturbation chosen had a sine squared shape with 2 cm width and 2 GHz amplitude over the larger valleys with 12 cm width and varying depths. When computing the differential time-of-flight for a probing frequency slightly above the perturbation, it was found that the contribution from the δf_{cut} vanishes below an experimental noise level at around a depth of 10 GHz on the larger valley.

To conclude, the skewness of the perturbation shape has a much higher order impact compared to the perturbation kurtosis. It is not the aim in this study for the moment, but if the skewness of the perturbation was of interest, the tunneling band can be investigated further to provide information on the width along the tunneling barrier, i. e. information on the perturbation's shape. The kurtosis of the perturbation, on the other hand, was inferred to significantly contribute to the observed signals. As such, it is recommended in future work in this topic to corroborate the study on the reconstruction techniques with information from the perturbation shape for the type of perturbation being investigated, be it from simulations, theory or from previous measurements from other diagnostics.

6. Reconstruction from database of perturbations

The simplest and most powerful approach to reconstruct the blind areas is to, firstly, create a database of perturbations and the respective additional time-of-flight caused by each perturbation, and then, use this database to compare to the experimental signal and identify the perturbation size. Other methods were tested that used a simpler description of the time-of-flight signature due to the perturbation, e.g. the integral of the additional time-of-flight over a given frequency band, or a few set of time-of-flight values for a few corresponding probing frequencies. These types

of solutions are limited to specific signal shapes and cannot be generalized. Recording the full perturbation signal over a broad frequency band also allows for the addition of multiple perturbation signatures, whatever are their signal's shapes.

The signal measured while probing across the perturbation is too complex to be considered in this step and therefore it is skipped. Consequently, the recorded additional time-of-flight due to the perturbation only starts at the probing frequency equals to the cut-off frequency at the end of the perturbation, thus this probing frequency is denoted f_{end}. Furthermore, this approach allows for building the database with signals simulated under the WKB approximation. Therefore, when using this database, as long as the full-wave effects are avoided in the experimental signal, the WKB approximation is valid. The usage of the WKB approximation to compute the signal in the database drastically simplifies the recorded signals and speeds up the computations, also allowing for a higher resolution in the solution's space.

The approach of creating a database of solutions is similar to developing a neural network to invert the perturbation signals, as it has been done for inverting the density profile [35]. The main difference to these approaches is that when creating the database, the user has full control of the input parameters and the output accuracy can be precisely verified, allowing for a more precise determination of the error bars around the solution found.

For simplicity, only one perturbation shape is used to compute the example database of this paper. Unlike in section 4, there is no requirement to assume smooth shapes for smooth implementations into the cutoff profile. Furthermore, the smooth start and end of the perturbation is already experimentally compatible to the non-perturbed profile. Therefore, the perturbation shape assumed to create the database is half period of a sine function. Additional shapes will be considered in future refinements to the reconstruction technique.

The database contains the excess time-of-flight versus probing frequency, due to the perturbation on the space of the following parameters: the probing frequency at the end of the perturbation (f_{end}); the local value of f_{ce}; the local gradient of the cut-off frequency profile (∇f_{cut}); the perturbation width; and the perturbation depth.

This approach is based on knowing the unperturbed signal and the perturbation width, both of which are estimated from the experimental signal. The chosen database signal is the excess time-of-flight because in this way the perturbation signature is independent of the profile before it. The unperturbed signal can be estimated by removing the perturbation signature and interpolating the remaining signal, or by using a previous sweep as a reference, as long as it is smooth and continuous over the frequency band of interest. The choice entirely depends on the current conditions of the signals being treated. The width of the perturbation can be observed directly from the experimental signal. The first step is to recognize the probing frequency at the end of the perturbation. In the case that the end of the perturbation is directly probed, the time-of-flight signal shows a minimum of a valley at exactly the end of the perturbation. The other possible cases are a perturbation end at the same probing frequency as the start of the perturbation, or the cut-off frequency of the end is below the one at the start. It is not straight forward to distinguish one case from the other, and unless there is any external input, the value for f_{end} can be assumed equal to the last probing frequency taken from the unperturbed signal, or equivalently, the initial probing frequency of the perturbation. After f_{end} is estimated, the perturbation width can be computed by assuming that the end position corresponds to the reconstructed profile position with the probing frequency equals to f_{end} when using the unperturbed time-of-flight signal for the profile reconstruction.

The two situations that can be out of the scope of this approach are: 1) the perturbation is too wide and the end frequency is so high that the excess time-of-flight from the perturbation has depleted; and 2) the perturbed signal strongly diverges at the perturbation and never returns close to the unperturbed case.

The signals of the excess time-of-flight due to the perturbation versus the probing frequency starting at f_{end} are then computed on the five dimensions of parameters. The computed bandwidth of probing frequency after the perturbation was set to be from 1 to 15 GHz, which is expected to normally be more than necessary. Due to the full-wave effects to be avoided, as discussed in section 4, the usable bandwidth may change at each specific application. Envisaging a broad domain of parameters within realistic conditions and encompassing various experimental scales, the database was computed within the domain of parameters given in table 1. This range of parameters enables application for both X and O mode measurements, since there is a broad domain of probing frequencies and local magnetic field (which can be assumed null for O mode applications).

Figure 14 shows two examples of the signals stored in the database for two fixed sets of parameters (f_{end}, f_{ce}, ∇f_{cut}, width). The only parameter that is left to be determined in the inversion process is the perturbation depth. Given the experimental signal from probing a perturbation, it can be compared to the database of signals and the signal with the best match will indicate the perturbation depth. For a good

Table 1. Boundary conditions of all parameters in the database of sine valley perturbations.

parameter	minimum value	maximum value
f_{end}	25 GHz	250 GHz
f_{ce}	0	250 GHz
∇f_{cut}	0	250 GHz/m
width	0.02 m	0.4 m
depth	1 GHz	30 GHz

precision in the estimated depth, the database must be computed with a good resolution in the parameters. This leads to a large database but fast reconstruction process of the blind area. If the desired application require a smaller database, interpolations can be used between the stored signals at the cost of increasing the reconstruction time of the blind area.

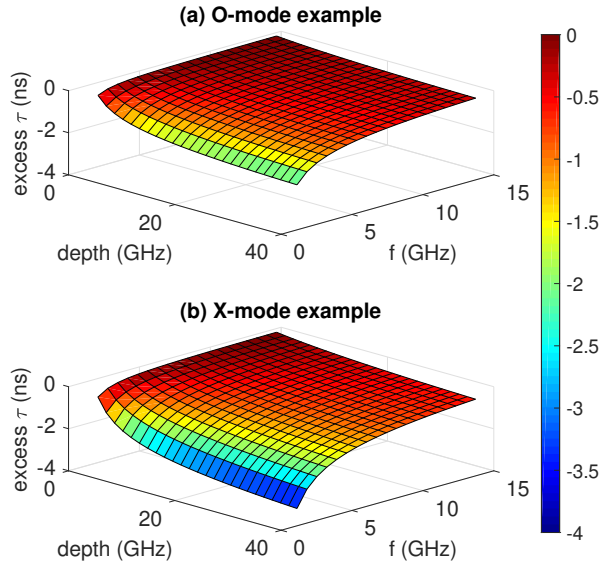

Figure 14. Example solutions of database of time-of-flight excess signals for sine shape valleys. Fixed parameters at (a): $width = 4cm$, $f_{end} = 40GHz$, $f_{ce} = 0$, $\nabla f_{cut} = 10GHz/m$. Fixed parameters at (b): $width = 4cm$, $f_{end} = 100GHz$, $f_{ce} = 60GHz$, $\nabla f_{cut} = 10GHz/m$.

After constructing the database, the first test performed was to apply the reconstruction technique to a blind area using noiseless synthetic data. The result obtained was very successful, equivalent to the case presented in figure 5.

The intrinsic physical resolution on the database to determine the depth of the perturbation is linked to the magnitude of the excess time-of-flight from the perturbation compared to the current noise level. A more detailed observation of the dependencies over the full range of parameters can be found in [25], but in summary, it was found that the resolution in depth increases with increasing width and decreasing depth. The dependency over f_{ce} is almost negligible compared to the other parameters. The resolution on depth increases with decreasing ∇f_{cut} and it is emphasized at wider perturbations. The last parameter, f_{end}, showed greater resolution at lower probing frequencies. After determining all parameters and reaching a given depth resolution physically intrinsic to the database, the experimental conditions of the extracted time-of-flight sets the final reconstruction accuracy, as will be observed in section 7.

7. Experimental demonstration of blind area reconstruction

This section aims to reconstruct the profile over a blind area based on all the results from the previous sections, only this time on an experimental case. The data used is from the Tore Supra database, shot 32029. The perturbation being investigated corresponds to a magnetic island on the $q = 2/1$ rational surface calculated from the equilibrium code [36]. Since the probing frequency sweep time for this shot was 20 μs, followed by a dead time of 5 μs, only a single sweep is used at a time because there is visible evolution of the perturbation between sweeps. The used frequency and amplitude signals around the perturbation are displayed in figure 15.

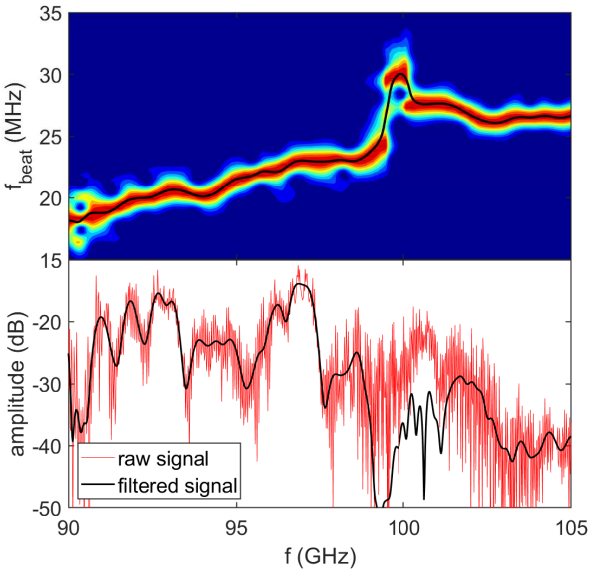

Figure 15. Beat frequency and amplitude signals around the perturbation to be investigated. Only a broad bandpass filter was applied to remove reflections that were far from the main branch. Tore Supra discharge 32029 at t = 3.0037 s.

Figure 15 shows around a probing frequency of 100 GHz the fluctuations of the beat frequency and of

the signal amplitude, which are caused by the density perturbation to be reconstructed. The indications of the perturbation are the discontinuity on the spectrogram and a strong drop in the amplitude signal in the respective probing frequencies, corresponding to the results from the full-wave simulations.

Only a broad (40 MHz) bandpass filter was applied in the beat frequency signal and the selected window size for the spectrogram was 90 points to ensure that the spectrogram shows the fast change in beat frequency. Figure 16 illustrates the time-of-flight signal of the perturbation compared to the reference unperturbed signal in white.

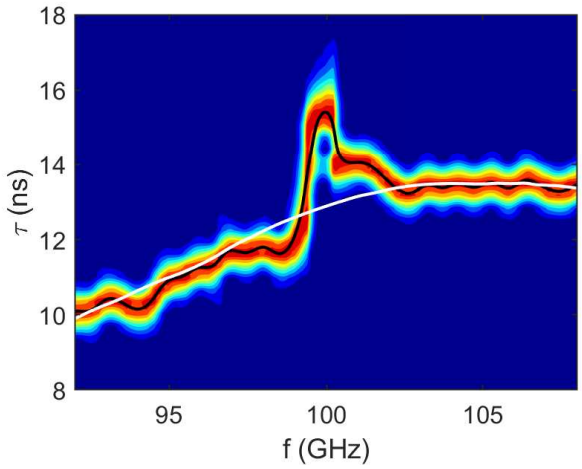

Figure 16. Time-of-flight signal around the perturbation of interest compared to the reference unperturbed case in white. Tore Supra discharge 32029, with the perturbation at t = 3.0037 s and the reference unperturbed case at t = 3.0033 s.

The magnetic islands typically appear with a positive density perturbation followed by a negative density perturbation. At least the first half of the positive perturbation can still be traditionally probed and reconstructed (first quarter of the entire perturbation). Therefore, in this case, instead of using a database of sine valleys, the perturbation shape follows the same shape as the positive part that is probed.

The signature for the perturbation end is always a dip in the time-of-flight signal when the perturbation end is exposed, or not visible when the end is not exposed (meaning that the positive part is in front of the end point). For the perturbation present is Fig. 16, there is no visible dip in the time-of-flight signal marking the perturbation end. In this specific case, the density perturbation could not end at the end of the perturbation signature, $\approx$ 102.5 GHz, because the respective f_R profile was verified to be very smooth and the perturbation would be so small that there wouldn't be a jump in time-of-flight, as observed in practice. Therefore, the perturbation end must be no greater than 100.2 GHz, which was the value assumed and led to a combined width of 6.1 cm. In any case, if the perturbation end is slightly before this value, the perturbation shape would not change significantly. With the width already estimated and the first quarter of the perturbation determined, the remaining three quarters of the perturbation retains the same shape and is squeezed or stretched to arrive at the estimated perturbation width.

The next step is to estimate the perturbation depth. The depth is extracted from comparing the experimental data against WKB simulated signals of various depths. In this case, the database constructed is already collapsed to the estimated set of parameters (shape, width, f_{ce}, ∇f_{cut}, f_{end}). As observed in section 4, the bandwidth where the signal's amplitude is low is considered dominated by full-wave effects and is skipped. In this case, the skipped band is from 98.5 GHz to 102.2 GHz. Figure 17 shows a comparison of the experimental signal of excess time-of-flight due to the perturbation to the simulated signals with different depths.

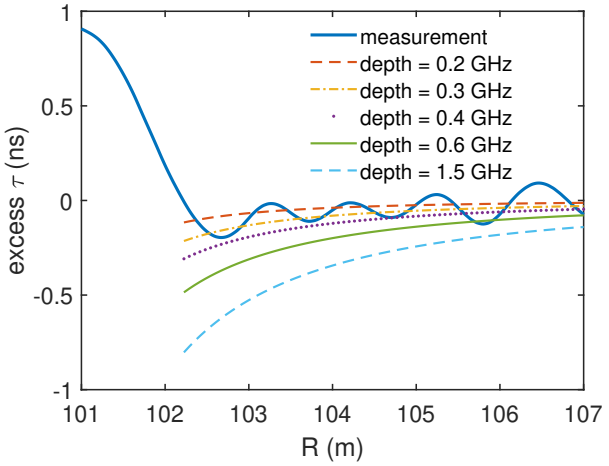

Figure 17. Comparison between the measured perturbation signal to WKB signals including the valley density perturbation with varying depth values.

From observing figure 17, the depths of 0.2 GHz and 0.4 GHz from the database synthetic signals are good indications of each limit of the possible perturbation depth. It leads to a final depth for the valley perturbation of 0.3$\pm$0.1 GHz, or equivalently, a perturbation of $5.0 \pm 1.7 \times 10^{17} m^{-3}$ and a local $\delta n_e = 2.4 \pm 0.8\%$. The resulting perturbation profile is depicted in figure 18 and the final density profile is given in figure 19, compared to the traditional reconstruction method on the perturbed and unperturbed measurements.

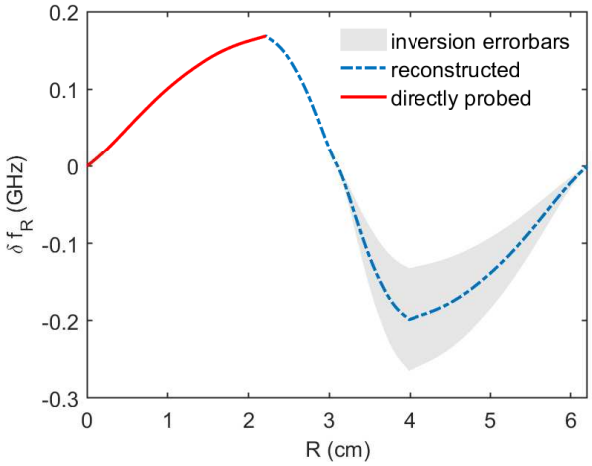

Figure 18. Complete perturbation in f_{cut} formed by a partially probed first quarter that is reflected to complete the bump and valley perturbations.

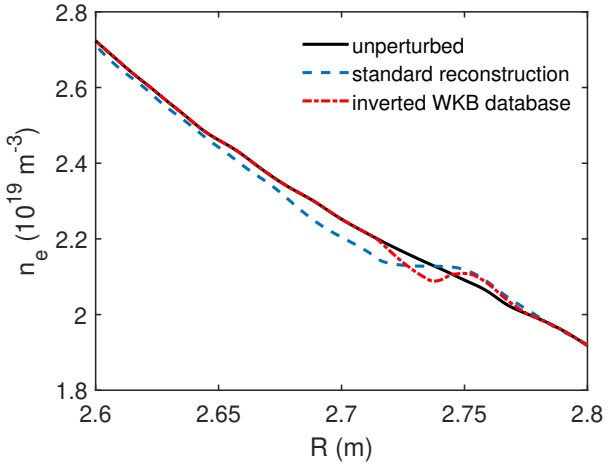

Figure 19. The reconstructed density profiles using the standard reconstruction method on the perturbed and unperturbed measurements versus the new method to reconstruct blind areas introduced in this paper.

It is clear from observing figure 19 that the new reconstruction scheme for the blind area describes much better the perturbation and eliminates a reminiscent tail of discrepancy.

8. Conclusions and future prospects

The reconstruction of blind regions in frequency swept reflectometry has never been tackled before. As it was demonstrated, the standard reconstruction process adds a significant error in the density profile if no special technique is applied around the perturbed region. The work presented here investigated more general characteristics to lay the foundations for this novel technique to improve the density profile.

Even though the main physical characteristics of the blind regions have been well described by the 1D simulations present in this contribution, future 3D simulations [37] will be necessary to verify any additional geometrical aspects. After all, the probing beam area and shape, plus the shape of the perturbations, make in conjunction a system too complex to be completely described in one dimension. These geometrical aspects influence the amplitude signal across the perturbation bandwidth and the appearance and dynamics of resonances. Understanding these effects will help to better extract the signals from the blind area, apply any phase correction due to the 3D structures and ultimately will lead to a more accurate employment of the database. This research on the geometrical aspects will also intersect with the research of improved initialization techniques.

The reconstruction technique of blind areas was verified to be very accurate in the absence of noise and with precise input of parameters when tested on synthetic data. Thus, the final reconstruction accuracy is expected to be related to the accuracy in which the perturbation width, shape and the local parameters of ∇f_{cut} and f_{ce} have been determined, which will vary significantly according to each application. As a first approximation, the constructed database assumed sine shaped valleys. If any other shape is of interest, the database can be recomputed for that specific shape, as it was demonstrated in the experimental example. In the end, a few different shapes can be available. Numerical or theoretical predictions can dictate which shape to be used in the database for a more accurate estimation of the perturbation depth on each specific application.

The estimations of perturbation width and ∇f_{cut} will degrade if there is only a single frequency sweep available with high amplitude low k perturbations, i.e. a case with low signal to noise ratio. For systems with faster sweeping rates, as achieved in ASDEX Upgrade and WEST with a 1 μs sweep time [38], there would be many sweeps at which the perturbation can be considered stationary. In such cases, the sum of many sweeps can help improve the signal to noise ratio to obtain a much better time-of-flight signal and consequently better assumptions of the perturbation width, the local ∇f_{cut}, and a more accurate extraction of the perturbation depth when compared to the database signals. Future applications will be investigated in dedicated contributions including more sophisticated statistical analysis of the database inversion process with such techniques and further analyses on the assumed perturbation shape.

Acknowledgments

This work has been carried out with the support of the Brazilian National Council for Scientific and Technological Development (CNPq) under the Science Without Borders programme and within the framework of the French Federation for Magnetic Fusion Studies (FR-FCM) and of the EUROfusion consortium with funding from the Euratom research and training programme 2014-2018 and 2019-2020 under grant agreement No 633053. The views and opinions expressed herein do not necessarily reflect those of the European Commission.

I also would like to thank F. Clairet for providing the experimental data from the Tore Supra database and for verifying the applied data treatment.

References

[1] Wang G, Zeng L, Doyle E J, Rhodes T L and Peebles W A 2003 *Review of Scientific Instruments* **74** 1525–1529
[2] Moreau P, Clairet F, M Chareau J, Paume M and Laviron C 2000 *Review of Scientific Instruments* **71** 74–81
[3] Clairet F, Sabot R, Bottereau C, Chareau J M, Paume M, Heuraux S, Colin M, Hacquin S and Leclert G 2001 *Review of Scientific Instruments* **72** 340–343
[4] Silva A, Manso M E, Cupido L, Albrecht M, Serra F, Varela P, Santos J, Vergamota S, Eusébio F, Fernandes J, Grossmann T, Kallenbach A, Kurzan B, Loureiro C, Meneses L, Nunes I, Silva F and Suttrop W 1996 *Review of Scientific Instruments* **67** 4138–4145
[5] Varela P, Manso M, Silva A, the CFN Team and the ASDEX Upgrade Team 2006 *Nuclear Fusion* **46** S693
[6] Sirinelli A, Alper B, Bottereau C, Clairet F, Cupido L, Fessey J, Hogben C, Meneses L, Sandford G, Walsh M J and JET-EFDA Contributors 2010 *Review of Scientific Instruments* **81** 10D939
[7] Clairet F, Bottereau C, Chareau J M and Sabot R 2003 *Review of Scientific Instruments* **74** 1481–1484
[8] Clairet F, Ricaud B, Briolle F, Heuraux S and Bottereau C 2011 *Review of Scientific Instruments* **82** 083502
[9] Briolle F, Lima R and Mendes R V 2009 *Measurement Science and Technology* **20** 105502
[10] Doyle E J 2015 Status of the system design and component testing for the ITER low-field side reflectometer system. 12th International Reflectometry Workshop, Jülich, Germany
[11] Heuraux S, Clairet F and da Silva F 2009 An X-mode reflectometry study on the reflection point for the density profile reconstruction Talk and proceeding at the 9th International Reflectometry Workshop, Lisbon, Portugal www.ipfn.tecnico.ulisboa.pt/irw9
[12] Hutchinson I H 2002 *Principles of Plasma Diagnostics* (UK: Cambridge University Press)
[13] Abel N H 2009 *Journal fur die reine und angewandte Mathematik* **1826** 153–157
[14] Bottollier-Curtet H and Ichtchenko G 1987 *Review of Scientific Instruments* **58** 539–546
[15] Bottollier-Curtet H 1986 *Réflectométrie hyperfréquence pour la détermination de la densité électronique et de ses fluctuations sur le Tokamak Petula-B* Ph.D. thesis Université de Paris XI
[16] Shelukhin D A, Vershkov V A, Sarychev D V, Petrov A A, Petrov V G and Subbotin G F 2011 X-mode lower cutoff high field side reflectometer for electron density profile measurements in T-10 tokamak 11th International Reflectometry Workshop, Palaiseau, France www.lptp.polytechnique.fr/news/11/Workshop/index.html
[17] B Morales R, Hacquin S, Heuraux S and Sabot R 2017 *Review of Scientific Instruments* **88** 043503
[18] Heuraux S, Hacquin S, da Silva F, Clairet F, Sabot R and Leclert G 2003 *Review of Scientific Instruments* **74** 1501–1505
[19] Gerbaud T, Clairet F, Sabot R, Sirinelli A, Heuraux S, Leclert G and Vermare L 2006 *Review of Scientific Instruments* **77** 10E928
[20] Fanack C, Boucher I, Clairet F, Heuraux S, Leclert G and Zou X L 1996 *Plasma Physics and Controlled Fusion* **38** 1915
[21] Sakamoto R, Pégourié B, Clairet F, Géraud A, Gil C, Hacquin S and Köchl F 2013 *Nuclear Fusion* **53** 063007
[22] Donné A J H, van Gorkom J C, Udintsev V S, Domier C W, Krämer-Flecken A, Luhmann N C and Schüller F C (TEXTOR team) 2005 *Phys. Rev. Lett.* **94**(8) 085001
[23] Baiocchi B, Bourdelle C, Angioni C, Imbeaux F, Loarte A, Maslov M and JET Contributors 2015 *Nuclear Fusion* **55** 123001
[24] Vayakis G, Walker C, Clairet F, Sabot R, Tribaldos V, Estrada T, Blanco E, Sánchez J, Denisov G, Belousov V, Silva F D, Varela P, Manso M, Cupido L, Dias J, Valverde N, Vershkov V, Shelukhin D, Soldatov S, Urazbaev A, Frolov E Y and Heuraux S 2006 *Nuclear Fusion* **46** S836–S845 URL `https://doi.org/10.1088%2F0029-5515%2F46%2F9%2Fs20`
[25] Morales R B 2018 *Density profile reconstruction methods for X-mode reflectometry* Ph.D. thesis Université de Lorraine URL `http://docnum.univ-lorraine.fr/public/DDOC_T_2018_0031_BIANCHETTI_MORALES.pdf`
[26] Conte S D and Boor C W D 1980 *Elementary Numerical Analysis: An Algorithmic Approach* (McGraw-Hill Higher Education)
[27] Colin M 2001 *Modelisations d'un reflectometre mode X en vue de caracteriser les fluctuations de densite et de champ magnetique: Applications aux signaux de Tore Supra* Ph.D. thesis Université de Lorraine
[28] Sabot R, Clairet F, Honoré C, Bottereau C, Chareau J M, Gabillet F, Hennequin P, Heuraux S, Leclert G, Sirinelli A, Truc A and Vermare L 2004 *International Journal of Infrared and Millimeter Waves* **25** 229–246 ISSN 1572-9559
[29] Clairet F, Heuraux S, Bottereau C, Molina D, Ducobu L, Leroux F and Barbuti A 2010 *Review of Scientific Instruments* **81** 10D903 – 10D903
[30] Heuraux S, Gusakov E, Popov A Y, da Silva F and Irzak M 2010 *IEEE Transactions on Plasma Science* **38** 2150–2158
[31] Budden K G 1966 *Radio Waves in the Ionosphere* (UK: Cambridge University Press)
[32] Gusakov E Z, Heuraux S and Popov A Y 2009 *Plasma Physics and Controlled Fusion* **51** 065018
[33] Moors J J A 1986 *The American Statistician* **40** 283–284
[34] Abramowitz M and (Eds) I A S 1972 *Handbook of Mathematical Functions with Formulas, Graphs, and Mathematical Tables, 9th printing* (New York: Dover Books on Mathematics)
[35] Santos J, Nunes F, Manso M and Nunes I 1999 *Review of Scientific Instruments* **70** 521–524
[36] Clairet F, Heuraux S, Leclert G and Vermare L 2005 FM-CW reflectometry for MHD activity measurements on Tore Supra Proc. 7th Intl. Reflectometry Workshop for fusion plasma diagnostics - IRW7 Garching, IPP Report II/9, p104
[37] da Silva F, Pinto M C, Després B and Heuraux S 2015 *Journal of Computational Physics* **295** 24 – 45 ISSN 0021-9991

[38] Clairet F, Bottereau C, Medvedeva A, Molina D, Conway G D, Silva A and Stroth U 2017 *Review of Scientific Instruments* **88** 113506